


## Photoresponsive characteristics of thin film transistors with perovskite quantum dots embedded amorphous InGaZnO channels

Mei-Na Zhang(张美娜), Yan Shao(邵龑), Xiao-Lin Wang(王晓琳), Xiaohan Wu(吴小晗), Wen-Jun Liu(刘文军), Shi-Jin Ding(丁士进)

**Citation:**Chin. Phys. B . 2020, 29(7): 078503 . **doi:** 10.1088/1674-1056/ab9738
Journal homepage: http://cpb.iphy.ac.cn; http://iopscience.iop.org/cpb

**What follows is a list of articles you may be interested in**

---

## High-performance midwavelength infrared detectors based on InAsSb nBn design

Xuan Zhang(张璇), Qing-Xuan Jia(贾庆轩), Ju Sun(孙矩), Dong-Wei Jiang(蒋洞微), Guo-Wei Wang(王国伟), Ying-Qiang Xu(徐应强), Zhi-Chuan Niu(牛智川)

Chin. Phys. B . 2020, 29(6): 068501 . **doi:** 10.1088/1674-1056/ab8377

## Ultraviolet irradiation dosimeter based on persistent photoconductivity effect of ZnO

Chao-Jun Wang(王朝骏), Xun Yang(杨珣), Jin-Hao Zang(臧金浩), Yan-Cheng Chen(陈彦成), Chao-Nan Lin(林超男), Zhong-Xia Liu(刘忠侠), Chong-Xin Shan(单崇新)

Chin. Phys. B . 2020, 29(5): 058504 . **doi:** 10.1088/1674-1056/ab8891

## Water-based processed and alkoxide-based processed indium oxide thin-film transistors at different annealing temperatures

Xu-Yang Li(栗旭阳), Zhi-Nong Yu(喻志农), Jin Cheng(程锦), Yong-Hua Chen(陈永华), Jian-She Xue(薛建设), Jian Guo(郭建), Wei Xue(薛唯)

Chin. Phys. B . 2018, 27(4): 048504 . **doi:** 10.1088/1674-1056/27/4/048504

## Electrical properties of zinc-oxide-based thin-film transistors using strontium-oxide-doped semiconductors

Wu Shao-Hang, Zhang Nan, Hu Yong-Sheng, Chen Hong, Jiang Da-Peng, Liu Xing-Yuan

Chin. Phys. B . 2015, 24(10): 108504 . **doi:** 10.1088/1674-1056/24/10/108504

## Positive gate-bias temperature instability of ZnO thin-film transistor

Liu Yu-Rong, Su Jing, Lai Pei-Tao, Yao Ruo-He

Chin. Phys. B . 2014, 23(6): 068501 . **doi:** 10.1088/1674-1056/23/6/068501

---

# Photoresponsive characteristics of thin film transistors with perovskite quantum dots embedded amorphous InGaZnO channels*

Mei-Na Zhang(张美娜)[1,†], Yan Shao(邵龑)[1,2,†], Xiao-Lin Wang(王晓琳)[1], Xiaohan Wu(吴小晗)[1,‡], Wen-Jun Liu(刘文军)[1], and Shi-Jin Ding(丁士进)[1,§]

[1] *State Key Laboratory of ASIC and System, School of Microelectronics, Fudan University, Shanghai* 200433, *China*
[2] *Center for Information Photonics and Energy Materials, Shenzhen Institutes of Advanced Technology, Chinese Academy of Sciences, Shenzhen* 518055, *China*

(Received 22 April 2020; revised manuscript received 21 May 2020; accepted manuscript online 28 May 2020)

Photodetectors based on amorphous InGaZnO (a-IGZO) thin film transistor (TFT) and halide perovskites have attracted attention in recent years. However, such a stack assembly of a halide perovskite layer/an a-IGZO channel, even with an organic semiconductor film inserted between them, easily has a very limited photoresponsivity. In this article, we investigate photoresponsive characteristics of TFTs by using $CsPbX_3$ ($X$ = Br or I) quantum dots (QDs) embedded into the a-IGZO channel, and attain a high photoresponsivity over $10^3$ A·W$^{-1}$, an excellent detectivity in the order of $10^{16}$ Jones, and a light-to-dark current ratio up to $10^5$ under visible lights. This should be mainly attributed to the improved transfer efficiency of photoelectrons from the QDs to the a-IGZO channel. Moreover, spectrally selective photodetection is demonstrated by introducing halide perovskite QDs with different bandgaps. Thus, this work provides a novel strategy of device structure optimization for significantly improving the photoresponsive characteristics of TFT photodetectors.

**Keywords:** perovskite quantum dots, a-IGZO, thin-film transistor, photoresponsive characteristics

**PACS:** 85.60.GZ, 81.07.Ta, 85.30.Tv, 81.05.Gc **DOI:** 10.1088/1674-1056/ab9738

## 1. Introduction

Amorphous In–Ga–Zn–O (a-IGZO) thin-film transistors (TFTs) exhibit high field effect mobility, excellent electrical uniformity, flexibility, and low-temperature process, and thus have been extensively investigated in display panels, flexible electronics, and UV detectors.[1–8] However, with respect to detections of visible lights, the a-IGZO TFTs often show limited responsivity because of a rather wide bandgap larger than 3 eV in a-IGZO.[1,2] To achieve significantly improved visible light detections, various light-absorbing materials have been introduced into the devices, including organic semiconductor,[9–13] two-dimensional materials,[14,15] inorganic quantum dots (QDs),[16–19] and halide perovskites.[20–30] Among them, the halide perovskites are of great interest due to their strong light absorption, long carrier diffusion length, low-cost process, high charge carrier mobility, and tunable bandgaps ($\sim$ 1.7–3.2 eV).[31–37] Therefore, the concept of a-IGZO/perovskite hybrid-based photodetectors has been proposed in recent years, and presents enhanced photosensitive performance.[20–24,26]

So far, the reported a-IGZO/perovskite hybrid-based photodetectors include two different device structures, i.e., a-IGZO-covered perovskite channel devices and perovskite-covered a-IGZO channel ones.[20–24,26] The former, in which perovskite nanowires are sandwiched between a-IGZO and gate dielectric, cannot operate like a transistor because of the gate field shielding effect. The latter with perovskite films or QDs on the back side of the a-IGZO channel can maintain relatively high field-effect mobility, however, their photoresponsiveness is still rather limited.[20–24,26]

In this work, we propose a hybrid channel consisting of inorganic halide perovskite (IHP) QDs embedded in the a-IGZO film for TFT photodetector applications, which is inspired by the rather good stabilities and high photoluminescence quantum yields of the IHP QDs.[33–35,38–43] Therefore, the fabricated devices exhibit superior photodetecting performance, including high photoresponsivity, excellent detectivity, and so on. In particular, tunable spectrally-selective photodetections of the devices are realized by introducing different bandgap QDs, and the underlying mechanisms are also discussed.[44,45]

## 2. Experimental details

### 2.1. Synthesis of IHP QDs at room temperature

The IHP QDs solution was synthesized at room temperature according to the method reported by Li *et al.*[46] Firstly, 0.1 mmol $PbBr_2$ and 0.1 mmol CsBr were dissolved in 2.5 mL dimethylformamide (DMF) in atmosphere. Oleic acid (OA,

*Project supported by the National Natural Science Foundation of China (Grant No. 61874029) and the National Key Technologies R&D Program of China (Grant No. 2015ZX02102-003).

†These authors contributed equally.
‡Corresponding author. E-mail: wuxiaohan@fudan.edu.cn
§Corresponding author. E-mail: sjding@fudan.edu.cn

© 2020 Chinese Physical Society and IOP Publishing Ltd 

0.25 mL) and oleylamine (OAm, 0.125 mL) were added to stabilize the precursor solution, then stirred till a transparent solution. Next, 1 mL of the mixture was quickly added to toluene (10 mL) during stirring. In order to obtain pure products, the $CsPbBr_3$ QDs precursor solution was added into 30 mL methyl acetate and centrifuged at 8000 rpm for 2 min. Finally, the precipitate $CsPbBr_3$ QDs were dispersed in n-hexane for further use.

The $CsPbI_3$ QDs solution was obtained though the displacement reaction of $CsPbBr_3$ QDs and $PbI_2$ solution. Firstly, 0.4 mmol $PbI_2$ was dissolved into 10 mL n-dodecane with 1 mL OA and 0.5 mL OAm, and was stirred till a transparent solution. Then, the $PbI_2$ solution and the above prepared $CsPbBr_3$ QDs solution were mixed in the same volume ratio, and the color change from green to red could be observed. The method of purification was the same as that for the $CsPbBr_3$ QDs solution.

### 2.2. Fabrication of IHP QDs-based hybrid TFTs

For the hybrid device fabrications, 80 nm $Al_2O_3$ gate dielectrics were deposited by atomic layer deposition using trimethylaluminum (TMA) and $O_2$ plasma as precursors on the highly doped p-type silicon wafers ($< 0.0015$ Ω·cm) at room temperature.[47] Next, 20 nm a-IGZO films were deposited on the top of $Al_2O_3$ by radio frequency (RF) sputtering using an $InGaZnO_4$ ceramic target. Subsequently, different light absorption layers were prepared as following: the $CsPbBr_3$ or $CsPbI_3$ QDs solution was coated on the surface of the a-IGZO films by spin coating at 1000 rpm for 30 s, followed by drying at room temperature for 24 h in $N_2$. Then, 20 nm a-IGZO films were deposited on the top of the light absorption layers of the QDs as aforementioned. Finally, 30 nm Ti/70 nm Au bilayer electrodes were prepared by electron beam evaporation and a lift-off method. The channel length and width were 10 μm and 40 μm, respectively. A control device (i.e., a-IGZO TFT) employed a single a-IGZO channel, and the other components were the same as mentioned above.

### 2.3. Characterization of materials and devices

UV–visible absorption spectra were measured on a UV–visible spectrophotometer (Lambda 750). Photoluminescence (PL) spectra were recorded by a spectrophotometer (F-320, Tianjin Gangdong Sci.&Tech. Co., Ltd). The x-ray diffraction (XRD) of the IHP QDs was collected by an x-ray diffractometer (Bruker Advance D8) with Cu $K\alpha$ radiation (1.54 Å) at 40 kV. The transmission electron microscopy (TEM) image and the surface morphologies of the IHP QDs films were observed by FEI Talos F200X and an atomic force microscope (AFM, Bruker Icon), respectively. The monochromatic lights of different wavelengths were provided by a xenon arc lamp filtered with a double grating monochromator (Omno 330150, Beijing NBeT, China). The electrical characteristics of the photodetectors were measured by an Agilent B1500A semiconductor device analyzer at room temperature in atmosphere.

## 3. Results and discussion

Figure 1(a) shows the TEM image of the representative $CsPbBr_3$ QDs, exhibiting an average size of around 5 nm and a highly crystalline texture. The XRD patterns of the $CsPbBr_3$ and $CsPbI_3$ QDs are presented in Fig. 1(b), indicating the formations of cubic $CsPbBr_3$ and $CsPbI_3$ phases.[33,35,36,48] As shown in Fig. 1(c), under an excitation wavelength of 365 nm, the emission peaks of the $CsPbBr_3$ and $CsPbI_3$ QDs are centered at 520 nm and 640 nm, respectively. The UV–Vis absorption spectra of the IHP QDs on a quartz substrate are illustrated in Fig. 1(d). The absorbance peaks of the $CsPbBr_3$ and $CsPbI_3$ QDs appear at about 490 nm and 630 nm, respectively.[49]

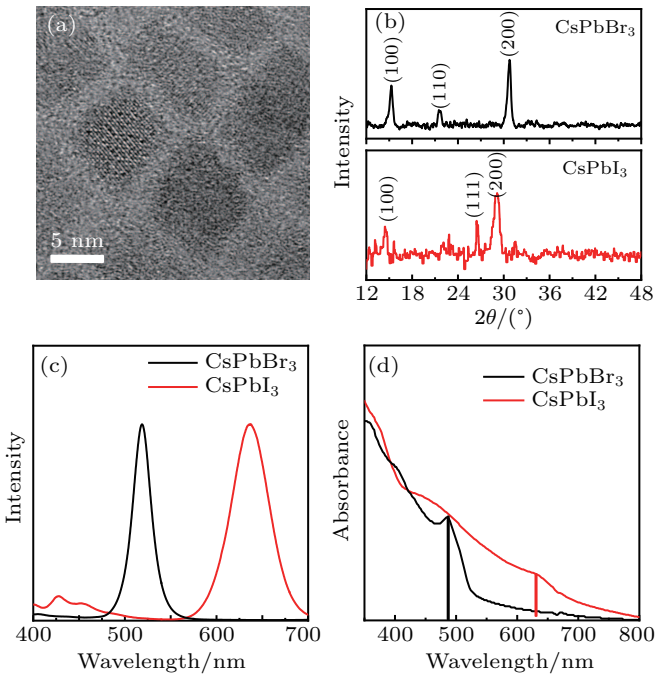



**Fig. 1.** (a) TEM image of the representative $CsPbBr_3$ QDs. (b) XRD patterns, (c) PL ($\lambda_{exc} = 365$ nm), and (d) optical absorption spectra of the $CsPbBr_3$ and $CsPbI_3$ QDs spin-coated on a quartz substrate.

Figure 2(a) shows the schematic diagram of the fabricated TFT photodetector with $CsPbX_3$ ($X$ = Br or I) QDs embedded a-IGZO channel (named as $CsPbX_3$-based hybrid TFTs), in which the highly doped p-type silicon substrate and $Al_2O_3$ film act as the back gate and dielectric, respectively; and the QDs as a light absorption medium are embedded in the middle of the a-IGZO layer, which can protect the QDs away from the atmosphere containing oxygen and moisture. The properties of the a-IGZO film deposited on the $Al_2O_3$ dielectrics by using the same RF sputtering method have been elaborately investigated previously, and the a-IGZO film exhibited small surface roughness and only a few oxygen vacancies.[47] The typical morphology of the QDs layer prepared via spin-coating is shown in Fig. 2(b), exhibiting a uniform and dense

distribution of the QDs. Furthermore, the energy band alignment of the $CsPbI_3$, $CsPbBr_3$, and a-IGZO is also presented in Fig. 2(c). Since a-IGZO has a bandgap beyond 3.25 eV, it is transparent to visible light.[1,2] In addition, the conduction band minimums ($E_c$) of both $CsPbI_3$ ($E_c = -3.6$ eV) and $CsPbBr_3$ ($E_c = -3.65$ eV) are higher than that of a-IGZO ($E_c = -4.3$ eV), so the photogenerated electrons from the $CsPbI_3$ or $CsPbBr_3$ QDs can transfer to the a-IGZO channel effectively. Furthermore, to demonstrate the superiority of the hybrid channel over the single a-IGZO one, the transfer characteristics of all the devices are compared, especially under different wavelength lights with a fixed power density ($P = 0.12$ mW/cm$^2$), as shown in Figs. 2(d)–2(f). The a-IGZO TFT demonstrates a very small threshold voltage ($V_T$) shift ($\sim 0.1$ V) under the 500 nm light, and almost no $V_T$ shift under the 540 nm light. This reveals that the single a-IGZO channel-based TFT cannot give active responses to the lights with a wavelength $\geq 500$ nm. Note that the drain currents for the a-IGZO TFT are extremely small when the gate voltages are between $-4$ V and $-1.5$ V, which are recorded as negative values, so that the transfer curves disappear in this region when an exponential coordinate axis is applied. Notably, both the $CsPbX_3$-based hybrid TFTs exhibit remarkable responses to different wavelength lights. In terms of the $CsPbBr_3$-based hybrid device, the drain current does not begin to increase gradually until the light wavelength is reduced from 700 nm to 580 nm (see Fig. 2(e)). However, for the $CsPbI_3$-based hybrid device, the resulting drain current always exhibits a gradual rise with decreasing the light wavelength from 700 nm to 500 nm (see Fig. 2(f) ). Such distinct responses to longer wavelengths (620–700 nm) for the latter should be ascribed to the smaller bandgap of the $CsPbI_3$ QDs. Briefly speaking, the adoption of the hybrid channel successfully extends the range of detectable light-wavelengths due to the incorporation of the $CsPbI_3$ or $CsPbBr_3$ QDs.

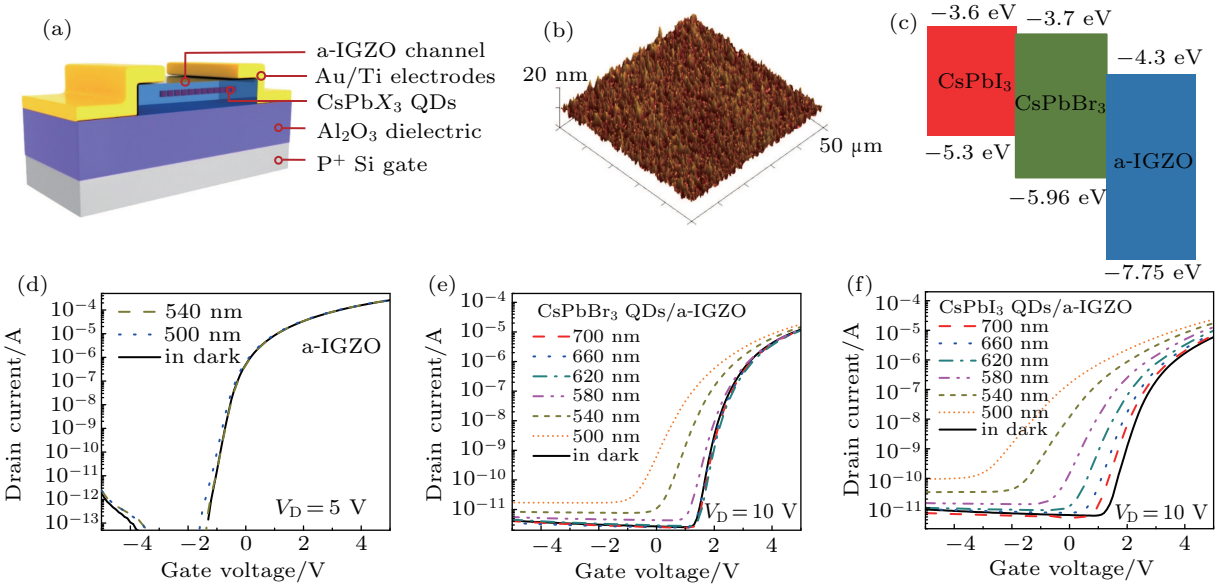



**Fig. 2.** (a) Schematic diagram of the TFT photodetector with $CsPbX_3$ ($X$ = Br or I) QDs embedded in the a-IGZO channel. (b) Typical AFM image of the $CsPbBr_3$ QDs layer. (c) Energy band alignment of $CsPbI_3$, $CsPbBr_3$, and a-IGZO. The transfer curves ($I_D$–$V_G$) of the TFTs under different wavelength lights ($P = 0.12$ mW/cm$^2$) as well as in the dark for (d) the single a-IGZO channel, (e) the a-IGZO/$CsPbBr_3$ QDs hybrid channel, and (f) the a-IGZO/$CsPbI_3$ QDs hybrid channel.

The transfer curves of both the $CsPbX_3$-based hybrid TFTs are further measured as a function of power density under 530 nm and 630 nm lights, respectively, as shown in Fig. 3. Under the 530 nm light, the $CsPbI_3$-based hybrid device exhibits a rapider increase in drain current than the $CsPbBr_3$-based one with the increase of the power density (i.e., 40 μW/cm$^2$ → 120 μW/cm$^2$), as shown in Figs. 3(a) and 3(b). Under the 630 nm light, the drain current as a function of the light power density for the $CsPbBr_3$-based hybrid device almost does not show any change (see Fig. 3(c)), but the drain current for the $CsPbI_3$-based hybrid device still exhibits an obvious rise with the increasing power density, as indicated in Fig. 3(d).

Further, the light power density-dependent threshold voltage ($V_T$) shifts and field effect mobility ($\mu$) are compared between the $CsPbBr_3$- and $CsPbI_3$-based hybrid TFTs, as displayed in Figs. 4(a) and 4(b). Regarding the $CsPbBr_3$-based device, both the $V_T$ shift and $\mu$ are almost stable with the increasing power density up to 120 μW/cm$^2$ under the 630 nm light, while they enlarge gradually as a function of the power density under the 530 nm light. With respect to the $CsPbI_3$-based device, both the $V_T$ shift and $\mu$ exhibit a gradual rise with the increasing power density under the 630 and 530 nm lights, respectively, and their change rates under the 530 nm light are much larger than those under the 630 nm light. Furthermore, the light wavelength-dependent $V_T$ shifts and $\mu$ are

shown in Figs. 4(c) and 4(d), respectively, for both the devices. It is found that the $CsPbI_3$-based hybrid device shows a gradual decrease in the $V_T$ shift and $\mu$, respectively, with the increasing light wavelength from 500 nm to 700 nm under the same power density. However, the $CsPbBr_3$-based hybrid device presents a gradual decrease in the $V_T$ shift and $\mu$ until the light wavelength increases to 620 nm, followed by unchanged values.

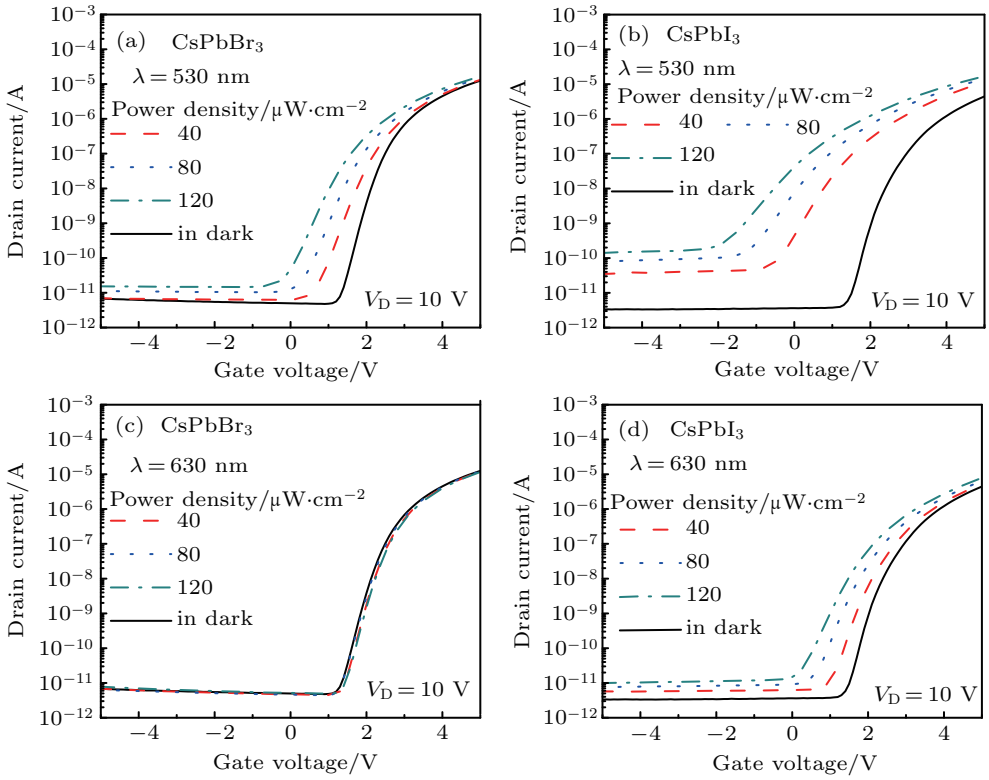



**Fig. 3.** The transfer curves ($I_D$–$V_G$) of a-IGZO/$CsPbBr_3$ QDs and a-IGZO/$CsPbI_3$ QDs hybrid TFTs under different light intensities with a constant wavelength of (a), (b) 530 nm or (c), (d) 630 nm.

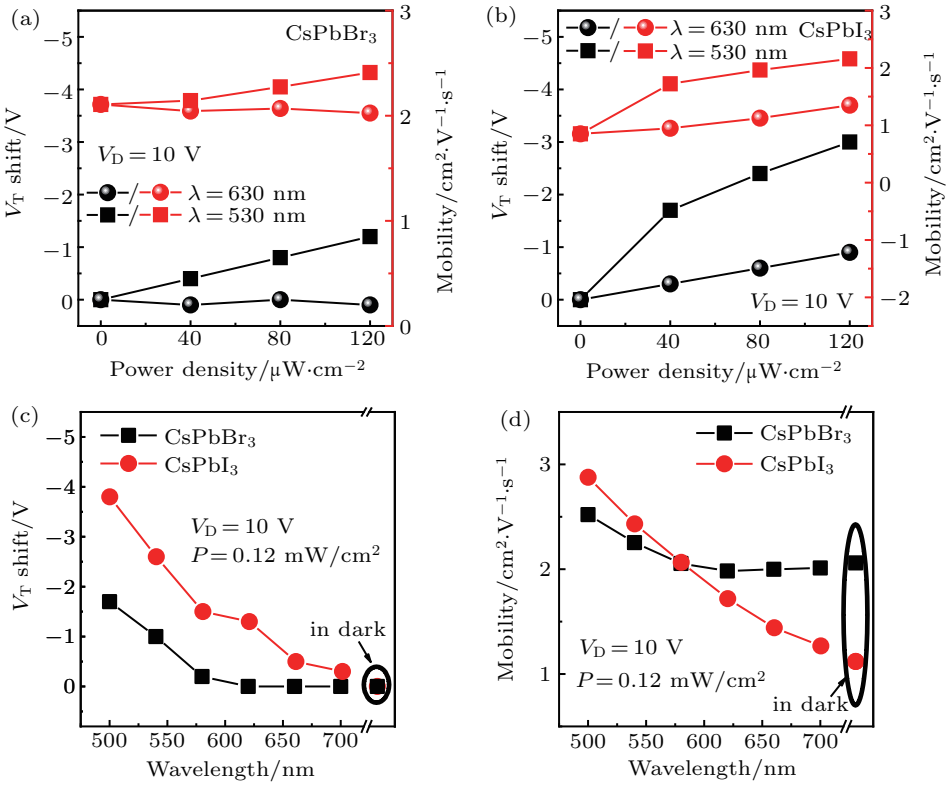



**Fig. 4.** Dependence of threshold voltage ($V_T$) shift and mobility on the power density of different wavelength light for (a) the $CsPbBr_3$-based hybrid TFT and (b) the $CsPbI_3$-based one. (c) The $V_T$ shifts and (d) mobility of the $CsPbBr_3$- and $CsPbI_3$-based hybrid TFTs as a function of light wavelength, together with those in dark.

In order to well evaluate the photosensitive characteristics of the TFT photodetectors, both photoresponsivity ($R$) and detectivity ($D^*$) are introduced, which can be calculated as[39,50,51]

$$R = \frac{I_{\text{light}} - I_{\text{dark}}}{P \cdot S}, \tag{1}$$

$$D^* = R\sqrt{\frac{S}{2eI_{\text{dark}}}}, \tag{2}$$

where $I_{\text{light}}$ and $I_{\text{dark}}$ represent the drain currents of the device under the light and in the dark, respectively; $P$ and $S$ correspond to the light power density and the effective illumination area (i.e., 40 μm×10 μm), respectively. Moreover, the ratio $I_{\text{light}}/I_{\text{dark}}$ is also an important parameter to evaluate the photodetector performance. Therefore, the gate voltage-dependent $R$ and $I_{\text{light}}/I_{\text{dark}}$ ratio are shown in Fig. 5 for the $CsPbBr_3$- and $CsPbI_3$-based hybrid TFT photodetectors under various wavelength lights while fixing the light power intensity at 120 μW/cm$^2$. It is found that the $CsPbI_3$-based hybrid device exhibits a larger $R$ than the $CsPbBr_3$-based counterpart under the same wavelength light and positive bias. Especially for the former, the $R$ value gradually rises with the increase of positive gate bias $V_G$ for a given light wavelength between 500 nm and 700 nm (see Fig. 5(b)). As the gate bias sweeps from −5 V to 5 V, $I_{\text{light}}/I_{\text{dark}}$ increases gradually to its maximum and then decays by some degrees for a constant light wavelength, as indicated in Figs. 5(c) and 5(d). Moreover, the maximum ratio of $I_{\text{light}}/I_{\text{dark}}$ gradually increases with the decreasing light wavelength from 700 nm to 500 nm. The maxima of both $R$ and $I_{\text{light}}/I_{\text{dark}}$ are plotted as a function of the light wavelength. For the $CsPbBr_3$-based hybrid device, the maxima of both $R$ and $I_{\text{light}}/I_{\text{dark}}$ decrease rapidly with the increasing light wavelength from 500 nm to 580 nm, and then approach to 0 and 1, respectively. This reflects that the hybrid device with $CsPbBr_3$ QDs cannot give photoresponses to the light with a wavelength ≥ 580 nm, i.e., it shows a wavelength-responsive cutoff of 550 nm. However, the $CsPbI_3$-based hybrid device exhibits a cutoff response to wavelength up to 700 nm, and the maxima of $I_{\text{light}}/I_{\text{dark}}$ and $R$ can be as large as $10^5$ and $10^3$ A·W$^{-1}$, respectively, under the 500 nm light and a gate bias of 5 V. Such results indicate that the spectrally responsive region of the hybrid TFT photodetector can be tuned by modulating the halide composition in the IHP QDs.

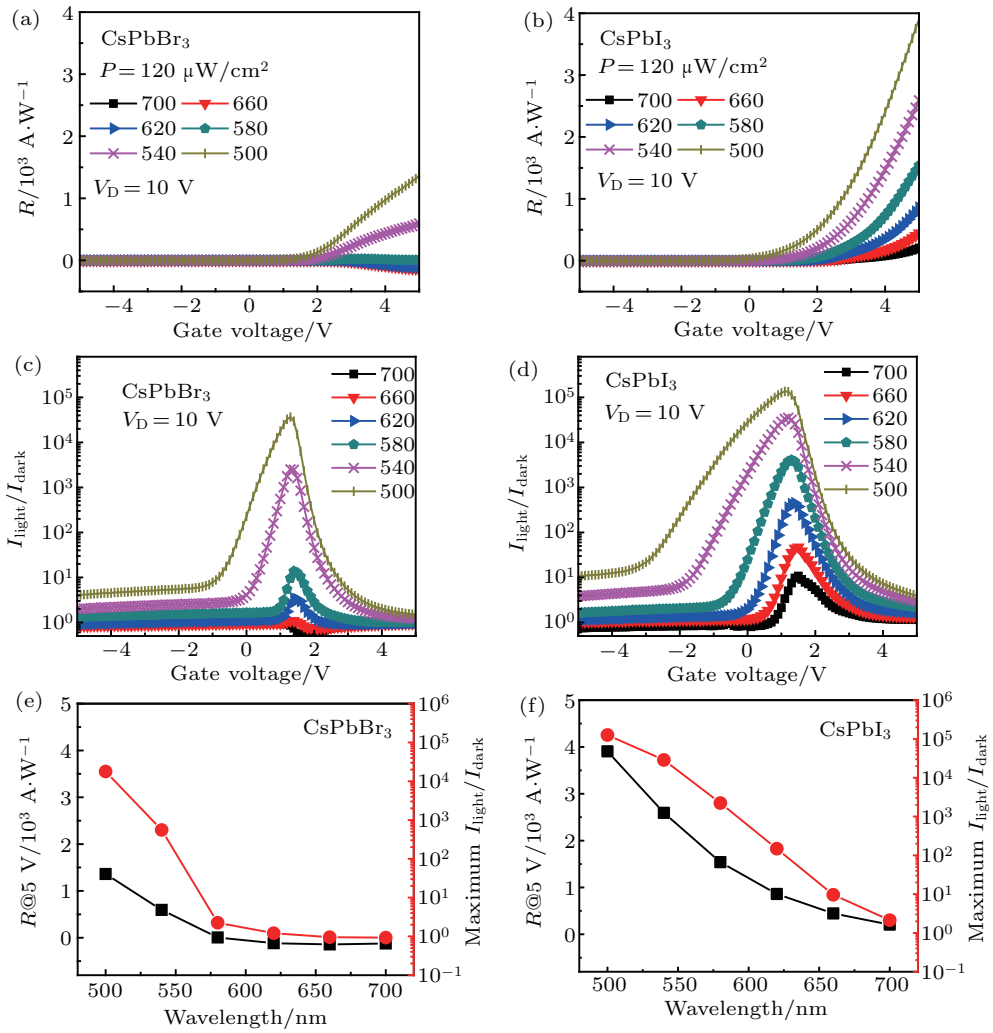



**Fig. 5.** (a), (b) Gate voltage-dependent $R$ and (c), (d) $I_{\text{light}}/I_{\text{dark}}$ ratio under different wavelength lights for the $CsPbBr_3$- and $CsPbI_3$-based hybrid TFTs, respectively. Dependence of $R$ ($V_G = 5$ V) and $I_{\text{light}}/I_{\text{dark}}$ maximum on light wavelength for (e) the $CsPbBr_3$-based hybrid device and (f) the $CsPbI_3$-based hybrid device.

Moreover, the transient response of the a-IGZO/$CsPbBr_3$ QDs hybrid TFTs to a switching light ($\lambda = 500$ nm) was investigated, as shown in Fig. 6(a). The photoswitching curve, including a photocurrent increase (Fig. 6(b)) and reduction (Fig. 6(c)) process, can be fitted with a double-exponential function[39,50]

$$\Delta I_{\rm D} = \Delta I_1 \left(1 - \exp(-t/\tau_1)\right) + \Delta I_2 \left(1 - \exp(-t/\tau_2)\right), \quad (3)$$

$$\Delta I_{\rm D} = \Delta I_3 \exp(-t/\tau_3) + \Delta I_4 \exp\left(-t/\tau_4\right), \quad (4)$$

where $\Delta I_{\rm D}$ is the variation of the drain current, and $\tau$ is the time constant. The time constants $\tau_1$ (0.11 s) and $\tau_3$ (0.27 s) correspond to photo carrier generation and recombination in the IHP QDs layer, while $\tau_2$ (0.86 s) and $\tau_4$ (1.67 s) represent the charge transfer time between the IHP QDs and the a-IGZO channel. The former is shorter than the latter, indicating that the photoresponse speeds are mainly dominated by the charge carrier transfer process.

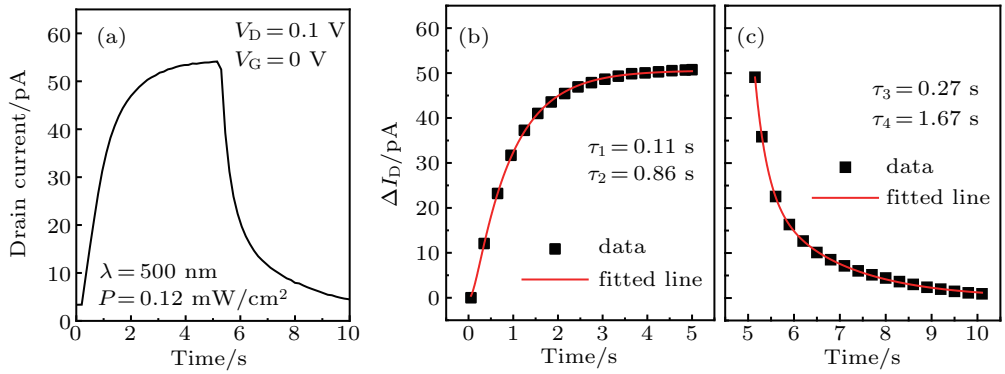



**Fig. 6.** (a) Photoswitching current curve of the a-IGZO/$CsPbBr_3$ QDs photodetector in dark and under illumination in an on/off cycle. The fitting line of the current during (b) on and (c) off switching.

Finally, the photoresponse mechanisms of the IHP QDs-based hybrid TFTs under different lights are expressed by schematic diagrams of energy band, as shown in Fig. 7. When a positive bias is applied to the gate of the a-IGZO TFT, electrons are accumulated in the a-IGZO channel due to downward bending of the a-IGZO energy band near the interface. Although the a-IGZO TFT is exposed to the 540 nm light, such a light cannot be absorbed by the a-IGZO channel because the energy of the 540 nm light (2.30 eV) is smaller than the bandgap of a-IGZO ($E_{\rm g} = 3.25$ eV). Thus, photogenerated carriers cannot be formed in the a-IGZO channel (see Fig. 7(a)), which makes the device be unable to respond to the 540 nm light, as indicated in Fig. 2(d). When the 540 nm light irradiates the $CsPbX_3$ ($X$ = Br or I)-based hybrid TFTs, it can be absorbed by $CsPbBr_3$ ($E_{\rm g} \sim 2.3$ eV) or $CsPbI_3$ ($E_{\rm g} \sim 1.7$ eV). Accordingly, lots of electrons are excited to the conduction band of the IHP QDs, thus producing free photoelectrons and leading to a photogating effect.[52] These photogenerated electrons further drift to the conduction band of the a-IGZO channel under the external electric filed, as shown in Fig. 7(b). Therefore, the photogating effect results in an increase of electron density in the channel, which reduces the $V_{\rm T}$ of the device, i.e., the $V_{\rm T}$ shifts towards a negative bias (see Figs. 2(e) and 2(f)). For a given wavelength light which can be absorbed by the IHP QDs, higher power density means that more photons per unit area can be absorbed, hence resulting in more photogenerated electrons in the channel. This thus gives rise to a gradually increased $V_{\rm T}$ shift in the direction of a negative bias with enhancing power density, as indicated in Figs. 4(a) ($\lambda = 530$ nm) and 4(b) ($\lambda = 530$, 630 nm). In addition, it is reported that some surface defects in the form of elemental vacancies usually exist on the IHP QDs. In our cases, the defects could be positive charged and thus act as electron traps in the QDs embedded a-IGZO channels.[53–55] Under effective illumination, the photogenerated electrons passivate the electron traps, i.e., the positive charged defects, at the interface of IHP QDs/a-IGZO, which is beneficial to improve the channel mobility likely due to the reduced Coulomb scattering effect, as shown in Fig. 4(d). On the other hand, the $V_{\rm T}$ shift and mobility decrease gradually as the incident light wavelength increases, as shown in Figs. 4(c) and 4(d) for the $CsPbI_3$-based hybrid TFT. This should be dominated by the change of visible light absorption in the $CsPbI_3$ QDs, as revealed in Fig. 1(d). When the light wavelength goes up to 620 nm (i.e., 2 eV), which cannot be absorbed by $CsPbBr_3$ ($E_{\rm g} \sim 2.3$ eV), photoelectrons cannot be easily produced in the $CsPbBr_3$ QDs (see Fig. 7(c)). In this case, the $CsPbBr_3$-based hybrid device can not any more give responses to the light with a wavelength $\geq 620$ nm, i.e., a wavelength cutoff of photoresponsivity appears, as suggested in Fig. 5(e). However, for the $CsPbI_3$-based hybrid device, the 620 nm light still can be absorbed by the $CsPbI_3$ QDs (see Fig. 7(d)), and thus good photoresponsivity is demonstrated till a wavelength of 700 nm, as revealed in Fig. 5(f).

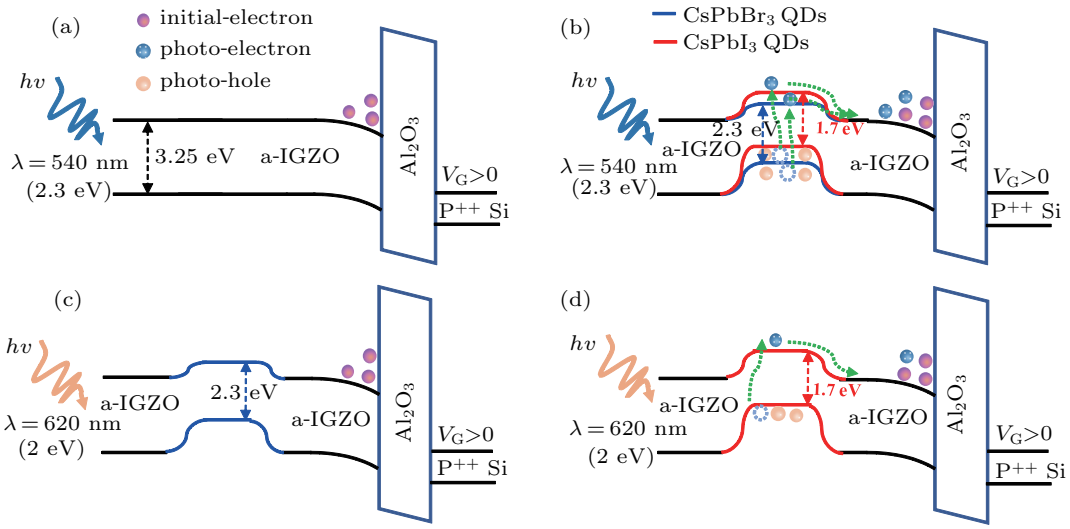



**Fig. 7.** Schematic diagrams of energy band for various devices under positive gate voltage: (a) the a-IGZO TFT under 540 nm light; (b) the $CsPbBr_3$- and $CsPbI_3$-based hybrid TFTs under 540 nm light; (c) the $CsPbBr_3$-based hybrid TFT under 620 nm light; (d) the $CsPbI_3$-based hybrid TFT under 620 nm light.

**Table 1.** Comparison of our $CsPbX_3$ ($X$ = Br or I)-based hybrid TFT photodetectors with reported others based on perovskite and a-IGZO. S/D represents source/drain, and PCBM means[6,6] –phenyl C61-butyric acid methylester.

| Device structure | Channel constitution (top-down) | $R$/A·W$^{-1}$ | $D^*$/Jones | $I_{light}/I_{dark}$ | $\mu$/cm$^2$·V$^{-1}$·s$^{-1}$ | Ref. |
|---|---|---|---|---|---|---|
| TFT (top S/D) | $CH_3NH_3PbI_3$ film/60 nm a-IGZO | 0.025 | $9.8\times10^9$ | – | 12.9 | [20] |
| TFT (top S/D) | $CsPbI_xBr_{3-x}$ film/20 nm a-IGZO | 26 | $8.42\times10^{14}$ | $8.71\times10^6$ | – | [24] |
| Heterostructure | 40 nm a-IGZO/$CsPbBr_3$ nanowires | 3.794 | – | $1.2\times10^4$ | – | [21] |
| TFT (top S/D) | $CH_3NH_3PbI_3$ film /50 nm a-IGZO | 61 | $9.42\times10^{10}$ | $3.48\times10^6$ | – | [22] |
| TFT (bottom S/D) | $CH_3NH_3PbI_3$ film/PCBM/40 nm a-IGZO | 0.01 | $1.35\times10^{12}$ | – | – | [23] |
| TFT (top S/D) | $CsPbBr_3$ QDs/PCBM/40 nm a-IGZO | 9.72 | $2.96\times10^{12}$ | $10^6$ | 8.95 | [26] |
| TFT (top S/D) | 20 nm a-IGZO/$CsPbBr_3$ QDs/20 nm a-IGZO | $1.4\times10^3$ | $1.0\times10^{16}$ | $3.7\times10^4$ | 2.52 | this work |
| TFT (top S/D) | 20 nm a-IGZO/$CsPbI_3$ QDs/20 nm a-IGZO | $3.9\times10^3$ | $1.7\times10^{16}$ | $1.4\times10^5$ | 2.87 | this work |

Table 1 compares our $CsPbX_3$ ($X$ = Br or I)-based hybrid TFT photodetectors with others based on perovskite and a-IGZO. Compared to the other channel constitutions, our $CsPbX_3$ ($X$ = Br or I) QDs embedded a-IGZO channels can provide much better photo-detecting properties, such as excellent $D^*$ ($1.0\times10^{16}$ or $1.7\times10^{16}$) and high $R$ (1400 A/W or 3900 A/W) under 500 nm illumination and a gate bias of 5 V. This should be attributed to a much higher transfer efficiency of the photoelectrons due to a shorter transfer distance between the perovskite QDs and the effective channel region. Moreover, compared with the heterostructure device, the amplifier function of the TFT photodetector also contributes to higher photoresponsivity.

## 4. Conclusion

Photodetectors based on a-IGZO TFT embedded with IHP QDs in the channel were successfully fabricated in this work, which exhibit excellent photosensitive performance with a photoresponsivity over $10^3$ A·W$^{-1}$, an $I_{photo}/I_{dark}$ of $10^5$, and a detectivity in the order of $10^{16}$ to visible light. The enhanced photoresponsivity, as compared with those of previously reported a-IGZO/perovskite hybrid devices, is mainly attributed to a higher transfer efficiency of the photoelectrons from the perovskite QDs to the effective channel region, as well as the amplifier function of the TFT. Moreover, the $CsPbBr_3$ and $CsPbI_3$ QDs embedded a-IGZO TFTs exhibit different wavelength-responsive cutoffs of 550 nm and 700 nm, respectively, indicating tunable spectrally selective photodetections. By optimizing the device structure, this work provides a novel strategy for further improving the performance of a-IGZO/perovskite hybrid photodetectors.

## References

[1] Nomura K, Ohta H, Takagi A, Kamiya T, Hirano M and Hosono H 2004 *Nature* **432** 488
[2] [2] Chuang C S, Fung T C, Mullins B G, Nomura K, Kamiya T, Shieh H P D, Hosono H and Kanicki J 2008 *Proc. Soc. Inf. Display* **39** 1215
[3] Kamiya T, Nomura K and Hosono H 2010 *Sci. Technol. Adv. Mater* **11** 044305
[4] Fortunato E, Barquinha P and Martins R 2012 *Adv. Mater.* **24** 2945
[5] Heremans P, Tripathi A K, de Jamblinne de Meux A, Smits E C, Hou B, Pourtois G and Gelinck G H 2016 *Adv. Mater.* **28** 4266
[6] Sheng J, Lee H J, Oh S and Park J S 2016 *ACS Appl. Mater. Interfaces* **8** 33821
[7] Zhang Y H, Mei Z X, Liang H L and Du X L 2017 *Chin. Phys. B* **26** 047307
[8] Xiao X, Zhang L, Shao Y, Zhou X, He H and Zhang S 2018 *ACS Appl. Mater Interfaces* **10** 25850
[9] Zan H W, Chen W T, Hsueh H W, Kao S C, Ku M C, Tsai C C and Meng H F 2010 *Appl. Phys. Lett.* **97** 203506
[10] Wang H, Xiao Y, Chen Z, Xu W, Long M and Xu J B 2015 *Appl. Phys. Lett.* **106** 242102
[11] Liu J, Wen H and Shen L 2020 *Nanotechnology* **31** 214001
[12] Xu Y and Lin Q 2020 *Appl. Phys. Rev.* **7** 011315

[13] Wang Y F, Qu F D, Zhou J R, Guo W B, Dong W, Liu C X, Ruan S P 2015 *Chin. Phys. Lett.* **32** 88504

[14] Yang J, Kwak H, Lee Y, Kang Y S, Cho M H, Cho J H, Kim Y H, Jeong S J, Park S, Lee H J and Kim H 2016 *ACS Appl. Mater. Interfaces* **8** 8576

[15] Pak S W, Chu D, Song D Y, Lee S K and Kim E K 2017 *Nanotechnology* **28** 475206

[16] Pei Z, Lai H C, Wang J Y, Chiang W H and Chen C H 2015 *IEEE Electron Device Lett.* **36** 44

[17] Shin S W, Lee K H, Park J S and Kang S J 2015 *ACS Appl. Mater. Interfaces* **7** 19666

[18] Hwang D K, Lee Y T, Lee H S, Lee Y J, Shokouh S H, Kyhm J h, Lee J, Kim H H, Yoo T H, Nam S H, Son D I, Ju B K, Park M C, Song J D, Choi W K and Im S 2016 *NPG Asia Mater.* **8** e233

[19] Weng Q C, An Z H, Xiong D Y and Zhu Z Q 2015 *Chin. Phys. Lett.* **32** 108503

[20] Du S, Li G, Cao X, Wang Y, Lu H, Zhang S, Liu C and Zhou H 2017 *Adv. Electron. Mater.* **3** 1600325

[21] Sun M, Fang Q, Zhang Z, Xie D, Sun Y, Xu J, Li W, Ren T and Zhang Y 2018 *ACS Appl. Mater Interfaces* **10** 7231

[22] Tak Y J, Kim D J, Kim W G, Lee J H, Kim S J, Kim J H and Kim H J 2018 *ACS Appl. Mater. Interfaces* **10** 12854

[23] Xu X, Yan L, Zou T, Qiu R, Liu C, Dai Q, Chen J, Zhang S and Zhou H 2018 *ACS Appl. Mater. Interfaces* **10** 44144

[24] Na H J, Cho N K, Park J, Lee S E, Lee E G, Im C and Kim Y S 2019 *J. Mater. Chem. C* **7** 14223

[25] Wei S, Wang F, Zou X, Wang L, Liu C, Liu X, Hu W, Fan Z, Ho J C and Liao L 2019 *Adv. Mater.* **32** 1907527

[26] Yu H, Liu X, Yan L, Zou T, Yang H, Liu C, Zhang S and Zhou H 2019 *Semicond. Sci. Technol.* **34** 125013

[27] Liu C K, Tai Q, Wang N, Tang G, Loi H L and Yan F 2019 *Adv. Sci.* **6** 1900751

[28] Wang Y, Song L, Chen Y and Huang W 2019 *ACS Photon.* **7** 10

[29] Zhao Y, Li C and Shen L 2019 *InfoMat* **1** 164

[30] Li C, Wang H, Wang F, Li T, Xu M, Wang H, Wang Z, Zhan X, Hu W and Shen L 2020 *Light Sci. Appl.* **9** 31

[31] Tiebin Yang F L, Rongkun Zheng 2019 *ACS Appl. Electron. Mater.* **1** 1348

[32] Zhang C, Kuang D B and Wu W Q 2020 *Small Methods* **4** 1900662

[33] Ramasamy P, Lim D H, Kim B, Lee S H, Lee M S and Lee J S 2016 *Chem. Commun.* **52** 2067

[34] Bi C, Wang S, Wen W, Yuan J, Cao G and Tian J 2018 *J. Phys. Chem. C* **122** 5151

[35] Bi C, Wang S, Li Q, Kershaw S V, Tian J and Rogach A L 2019 *J. Phys. Chem. Lett.* **10** 943

[36] Lao X, Li X, Agren H and Chen G 2019 *Nanomaterials* **9** 172

[37] Wang Y, Gao M L, Wu J L, Zhang X W 2019 *Chin. Phys. B* **28** 18502

[38] Chen W, Hao J, Hu W, Zang Z, Tang X, Fang L, Niu T and Zhou M 2017 *Small* **13** 1604085

[39] Chen Y, Chu Y, Wu X, Ou-Yang W and Huang J 2017 *Adv. Mater.* **29** 1704062

[40] Davis N J, de la Pena F J, Tabachnyk M, Richter J M, Lamboll R D, Booker E P, Wisnivesky Rocca Rivarola F, Griffiths J T, Ducati C, Menke S M, Deschler F and Greenham N C 2017 *J. Phys. Chem. C Nanomater Interfaces* **121** 3790

[41] Yu Y, Zhang Y, Song X, Zhang H, Cao M, Che Y, Dai H, Yang J, Zhang H and Yao J 2017 *Adv. Opt. Mater.* **5** 1700565

[42] Cai Z, Li F, Xu W, Xia S, Zeng J, He S and Chen X 2018 *Nano Res.* **11** 1447

[43] Liao J F, Xu Y F, Wang X D, Chen H Y and Kuang D B 2018 *ACS Appl. Mater. Interfaces* **10** 42301

[44] Jiang D W, Xiang W, Guo F Y, Hao H Y, Han X, Li X C, Wang G W, Xu Y Q, Yu Q J and Niu Z C 2016 *Chin. Phys. Lett.* **33** 48502

[45] Yong W, Hao L, You L X, Lv C L, Wang H Q, Zhang X Y, Zhang W J, Zhou H, Zhang L, Yang X Y and Wang Z 2019 *Chin. Phys. B* **28** 78502

[46] Li X, Yu D, Cao F, Gu Y, Wei Y, Wu Y, Song J and Zeng H 2016 *Adv. Funct. Mater.* **26** 5903

[47] Shao Y, Wu X, Zhang M N, Liu W J and Ding S J 2019 *Nanoscale Res. Lett.* **14** 122

[48] Fang Y, Dong Q, Shao Y, Yuan Y and Huang J 2015 *Nat. Photon.* **9** 679

[49] Song J, Xu L, Li J, Xue J, Dong Y, Li X and Zeng H 2016 *Adv. Mater.* **28** 4861

[50] Chen Y, Wu X, Chu Y, Zhou J, Zhou B and Huang J 2018 *Nanomicro Lett.* **10** 57

[51] Ma X F, Huang Y Q, Zhi Y S, Wang X, Li P G, Wu Z P and Tang W H 2019 *Chin. Phys. B* **28** 88503

[52] Fang H and Hu W 2017 *Adv. Sci.* **4** 1700323

[53] Long L, Cao D, Fei J, Wang J, Zhou Y, Jiang Z, Jiao Z and Shu H 2019 *Chem. Phys. Lett.* **734** 136719

[54] Azpiroz J M, Mosconi E, Bisquert J and De Angelis F 2015 *Energy Environ. Sci.* **8** 2118

[55] Podzorov V and Gershenson M E 2005 *Phys. Rev. Lett.* **95** 016602